Why ionizing radiation enhances surface wettability

SAND2020-2747J

Arunkumar Seshadri[a] *, Eric C. Forrest*[b]*, Koroush Shirvan*[a]*

[a]Department of Nuclear Science and Engineering, Massachusetts Institute of Technology, 24-215a, 77 Massachusetts Avenue, Cambridge MA-02139

[b]Sandia National Laboratories, P.O. Box 5800, Albuquerque, New Mexico 87185-0665

Abstract

Radiation-Induced Surface Activation is an inherent phenomenon where surfaces that are exposed to gamma irradiation are observed to undergo an increase in wettability. This increase in wettability as a result of the ionizing radiation exposure has so far been demonstrated to have a pronounced impact on Leidenfrost temperature and two-phase fluid dynamics. Test results from previous experiments have shown that incorporation of this effect on heat transfer equipment design may increase the thermal-hydraulic margin leading to higher thermal efficiency. However, the mechanism behind the increased wettability is not clearly understood. In the present work, three different materials (Zircaloy-4, 316 stainless steel, and copper) were exposed at two different dose rates with use of two different gamma irradiation facilities. A detailed surface characterization on the post-irradiated samples is carried out to understand the changes in surface chemistry, wettability and surface morphology. It is observed from the experiments that the increase in wettability upon irradiation depended on the total dose and not on the dose rate. Moreover, localized oxidation and porosity induced by radiolysis was seen to be the predominant mechanism behind increased wettability which leads to improved Leidenfrost temperature.

Keywords: Gamma irradiation, Hydrophilicity, Wettability, Oxidation, Surface energy, Radiation-induced surface activation

Introduction

Two-phase heat transfer (boiling and condensation) commonly occurs in various heat transfer equipment such as heat pipes used to cool power amplifiers, photovoltaics and integrated circuits as well as in various refrigeration and cryogenic systems.[1-5] Boiling is the dominant mode of heat transfer in boiling water reactors (BWRs).[6, 7] Two-phase heat transfer also occurs during quenching of core rodlets in light water reactors observed during the emergency cooling of reactors as well as in heat treatment of various materials.[8, 9] Two-phase heat transfer is limited by various phenomena such as critical heat flux (CHF) [10-12] and Leidenfrost temperature.[13-15] During the heating of surfaces, beyond critical flux, the heated surface is environed by a vapor blanked, drastically reducing the heat transfer from the surface.[16, 17] Similarly, in the cooling of materials, accelerated cooling is observed when the temperature drops below the Leidenfrost temperature, the point at which the film covering the heated surface collapses into bubbles that support faster cooling of surfaces.[18, 19]

Understanding mechanisms affecting boiling heat transfer helps in the development of advanced surfaces for enhancing CHF and Leidenfrost temperature as well as enabling better modeling of systems to accurately determine the thermal-margin for the operation of the heat transfer devices.[17, 20-25] Several analyses so far have determined that surface effects play a vital role in improving two-phase heat transfer as well as the heat transfer limits (CHF and Leidenfrost temperature).[11, 26-38] The major surface characteristics that affect boiling heat transfer include surface wettability [28], surface roughness [27, 39], and porosity [40, 41]. Increased surface roughness and porosity are known to affect the nucleation site distribution which in-turn impacts the onset of nucleate boiling.[42-44] It has also been shown that surface roughness contributes to the liquid-vapor interfacial instabilities leading to improved CHF and Leidenfrost temperature.[9,

27, 45-47] Porous surfaces also possess a higher water absorption capability to know as capillary wicking, which, leads to increased boiling heat flux as well as CHF.[48-54] Recently, an interesting mechanism on the early evaporation of the microlayer as a result of surface texture was also reported to enhance boiling heat transfer and CHF.[55] These pronounced impacts of surface characteristics on boiling heat transfer have lead researchers to focus on understanding the governing mechanisms as well as explore various ways to improve these surface characteristics to achieve a higher heat transfer rate. Recently, the authors proposed the need to develop a comprehensive model for two-phase heat transfer dynamics which depend on various surface parameters such as roughness, porosity, contact angle, and surface emissivity.[56]

Apart from surface roughness and porosity, surface wettability is seen to play a decisive role in determining boiling characteristics. Surface wettability is measured in terms of contact angle.[57] Contact angle (CA), which is the angle formed by the liquid-vapor interface with the test surface, is a complex function of surface chemistry as well as surface morphology, in addition to fluid-surface interaction parameters [57]. A decreased contact angle implies increased wettability. Though CA measurement is a common technique to measure wettability, the technique is no longer applicable in the case of superhydrophillic textured surfaces [58]. In hydrophilic non-ideal surfaces with roughness [59], the wetting behavior is described by the Wenzel state. In the Wenzel state, the liquid is in full contact with the solid surface penetrating into the surface textures and the measured CA becomes a function of its surface roughness. Such surface tend to move to a saturated Wenzel regime when the surface roughness becomes higher than the characteristic saturated roughness [58, 60]. In such cases, CA is always 0° as predicted by Wenzel state [61] and does not comprehensively capture the capillarity and interface effects. An alternative measurement technique utilized in this work to partially overcome such limitation is capillary wicking [49].

Hydrophobic surfaces (CA>90°) [59] are preferred to accelerate the onset of nucleate boiling which helps in achieving a higher heat transfer rate following the occurrence of boiling on heated surfaces [49]. However, hydrophilic surfaces are preferred to improve CHF as well as Leidenfrost temperature as these improve liquid contact with the surface [49]. Several methods have so far been developed to improve the wettability of surfaces, which include the development of nanostructures, application of coatings and use of photocatalyst such as ultraviolet (UV) rays. [62-69]. An interesting method presented by Zupančič, et al. [38] uses pulsed Nd: YAG laser to generate biphilic patterned surfaces which provide up to 200% simultaneous enhancement in two-phase heat transfer coefficient as well CHF. In fact, nanosecond laser texture is a robust means of engineering surfaces for enhanced heat transfer and was observed to work on fluids and mixtures of different polarity and fluid properties [36, 37, 70].

Gamma radiation is known to affect surface wettability through a phenomenon called radiation-induced surface activation.[71-74] Due to its scalability, Gamma irradiation can be effectively used to increase surface wettability in manufacturing and bio-medical industries where other techniques to improve wettability are difficult to implement. The importance of the effects of gamma irradiation is more readily realized in thermal hydraulics of nuclear reactors. The fission process governing energy generation in these reactors results in the creation of strong gamma fields that remain in the fuel cladding for decades via decay of the fission products. Few studies have so far been conducted to understand the effect of gamma irradiation. In the studies by Takamasa et al. [75], the contact angle was found to decrease in the case of gamma-irradiated metal oxide samples indicating an increase in surface energy for a period of time before the surface returned to its nominal condition. In yet another study, gamma irradiation was shown to increase the nucleation site density thereby affecting the critical heat flux on surfaces.[76] At least 20%

enhancement in CHF is observed in these studies conducted with various oxide surfaces. Recently, the authors have demonstrated that non-oxidized surfaces also show improved wettability when exposed to gamma radiation leading to significant enhancement in the Leidenfrost temperature.[77] It was also demonstrated that the mechanism behind increased wettability was different from that of UV induced hydrophilicity and there was a significant possibility of surface oxidation during gamma irradiation compared to UV-ozone treatments.

However, there is a need to completely understand the impact of the mechanism of gamma radiation-induced hydrophilicity by studying the effect of cumulative dose and rate of exposure. Surface morphology is known to be highly impacted by ionizing irradiation [78-88]. The change in surface characteristics as a result of radiation exposure and its role in interfacial energy transfer for various surfaces should be addressed. In the present work, a comprehensive post-irradiation surface examination of different surfaces when exposed to irradiation at two different dose rates is performed. The post-irradiation examination involves the use of advanced techniques for surface energy measurement, electron microscopy, and X-ray-based surface chemistry analysis. The effect of corrosion potential with gamma irradiation is also highlighted. Further, the effect of total dose on Leidenfrost temperature change is also studied.

Experimental setup and Methods

Gamma Irradiation

Two different gamma irradiators were used in the present work to irradiate the samples. The high dose rate Gamma Irradiation Facility (GIF) at Sandia National Laboratories provided a dose rate of 32 Gy/s. A picture of the gamma irradiation cell setup and the sample loading is shown in Figure 1. The gamma cell facility at MIT is used for exposure at a lower dose rate (present rate

~0.7 Gy/s). Both the cells use cobalt-60 as the source. The maximum absorbed dose in the sample in a single insertion is 19.2 MGy in the high dose rate facility and that applied in the low dose rate facility is 1.2 MGy. The dose rate was measured at the high dose rate facility using a calibrated Victoreen Model 550 Series cylindrical 0.3 cm^3 ionization chamber with the Inovision Radiation Measurements Therapy Dosimeter Model 35040 electrometer.

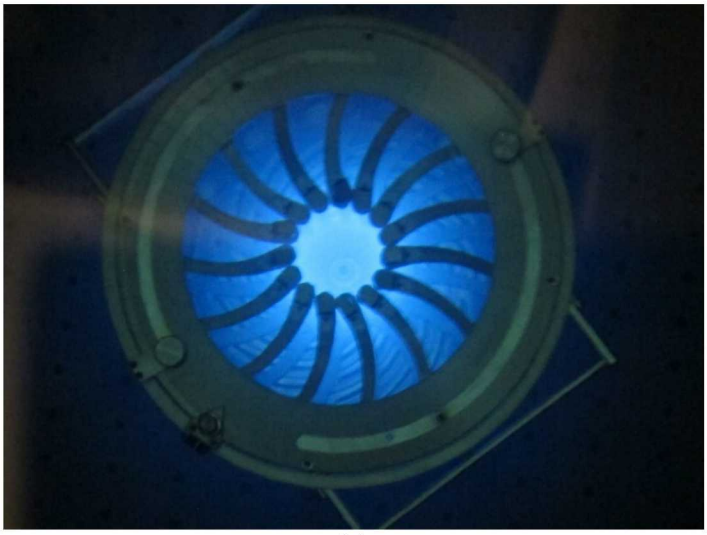

(a)

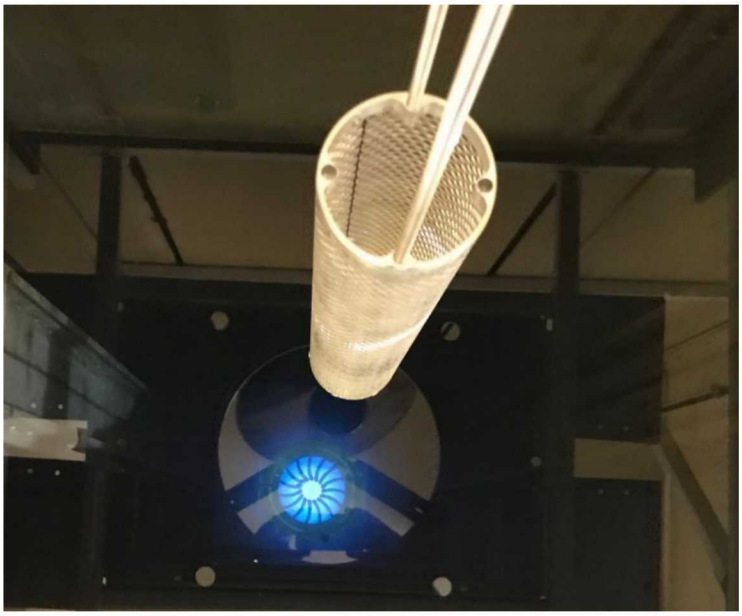

(b)

Figure 1. Cobalt-60 source: GIF Facility, (a) Cobalt-60 Source Array Used at the GIF. (b) Aluminum Sample Basket and Co-60 Array (submerged).

Wettability and Surface Energy Measurement

The surface energy of substrates was quantified through contact angle measurement on a Krüss DSA30 drop shape analyzer. Krüss DSA4 v. 2.0 software was used for contact angle analysis. The contact angle that a liquid makes with a solid interface depends on the surface tension of the liquid (typically denoted by σ) and the free surface energy of the solid, γ_s. From a force balance, the intrinsic contact angle may be related using the following expression, which was first described qualitatively by Young [89]

$$cos\theta_I = \frac{\gamma_{sv} - \gamma_{sl}}{\sigma} \quad (1)$$

where γ_{sv} is the solid-vapor interfacial tension (sometimes referred to as the surface tension of the solid in equilibrium with the vapor), γ_{sl} is the solid-liquid interfacial tension, and σ is the surface tension of the liquid (liquid-vapor interfacial tension, also represented as γ_{lv}). γ_{sv}-γ_{sl} is often referred to as the adhesion tension of the liquid/vapor/solid combination.

Later, the work by Dupré on adhesion between two immiscible liquids Dupré and Dupré [90] may be combined with Young's equation to obtain what is commonly referred to as the Young-Dupré equation:

$$W_{sl} = \sigma[1 + \cos(\theta)] \quad (2)$$

where W_{sl} is the work of adhesion per unit surface area, and the spreading pressure, $\pi_e=\gamma_s-\gamma_{sv}$ has been neglected, i.e., $\gamma_s=\gamma_{sv}$ and $\gamma_l=\gamma_{lv}=\sigma$. For the surface energy analysis in this study, spreading pressure will be neglected. Note that the units of surface energy (mJ/m^2) are equivalent to that of surface tension (mN/m).

The three-liquid approach is typically use to determine surface energy through the determination of the polar (Lewis acid-base) and Lifshitz-van der Waals (includes Debye, Keesom, and London dispersion interaction) components of the surface energy.[91] In this study, we utilize a four-liquid approach to improve the fidelity of the line fitment to the system of transcendental equations. Specifically, deionized water (>18 MΩ-cm), ethylene glycol (anhydrous, 99.8%, Sigma-Aldrich), glycerol (Molecular Biology Reagent, Sigma-Aldrich), and diiodomethane (ReagentPlus, Sigma-Aldrich) are employed. Selection of entirely nonpolar fluids is difficult, as most typically have low surface tensions and perfectly wet surfaces. Diiodomethane is a good candidate for a nonpolar liquid due to its high surface tension, leading to measurable contact angles in many cases. Surface tension values for the liquids utilized in this study are summarized in Table 1. Note that the default liquid surface tension database in the Krüss DSA4, v. 2.0 software had several errors. These values were corrected with those listed in Table 1 prior to performing the analysis. Droplet size depended on the liquid being dispensed but was typically between 1 μL and 5 μL.

Table 1. Contact angle liquid surface tension parameters for surface energy calculations.

	Total, γ (mN/m)	**Dispersive (Lifshitz van der Waals) γ^D or γ^{LW} (mN/m)**	**Polar (Acid-Base) γ^P or γ^{AB} (mN/m)**	**Acid γ^+ (mN/m)**	**Base γ^- (mN/m)**	**Source**
Water:	72.80	21.80	51.00	25.50	25.50	Bellon-Fontaine et al.Bellon-Fontaine, et al. [92]
Ethylene Glycol:	48.00	29.00	19.00	3.00	30.10	Oss et al.[93]
Glycerol:	64.00	34.00	30.00	3.92	57.38	Oss et al.[93]
Diiodo-methane:	50.80	50.80	0.00	<0.1	<0.1	Bellon-Fontaine et al.Bellon-Fontaine, et al. [92]

Two models for relating measured contact angle and liquid surface tension to the surface energy were explored. The first model divides the surface energy into a polar and a dispersive component, and is often attributed to Owens and Wendt [94] although Girifalco and Good introduced the model a decade earlier.[95]

$$\frac{\gamma_l(1+\cos\theta)}{2\sqrt{\gamma_l^D}} = \left(\frac{\gamma_l^P}{\gamma_l^D}\right)^{1/2}\sqrt{\gamma_s^P} + \sqrt{\gamma_s^D} \qquad (4)$$

Acid-base theory breaks the surface energy into a Lifshitz-van der Waals (dispersive) component, and an acid-base (polar) component.[96] The acid-base component of surface energy is further divided into the Lewis acid (electron acceptor) and Lewis base (electron donor) constituents. The model for acid-base theory is expressed as follows:

$$\gamma_l(1 + cos\,\theta) = 2\left[\sqrt{\gamma_s^{LW}\gamma_l^{LW}} + \sqrt{\gamma_s^{+}\gamma_l^{-}} + \sqrt{\gamma_s^{-}\gamma_l^{+}}\right] \quad (5)$$

The Krüss software solves the system of equations (in our study, four equations given the four unique liquids used). Four independent measurements were made on substrates with each fluid in order to assess repeatability (Type A uncertainty). Type B uncertainty for contact angle measurement was typically ± 2.0° based on the goniometer and contact angle fit in the software. All the contact angle presented in the work are static contact angle measurements. However rigorous measurement of CA would involve measurement of advancing and receding contact angles to eliminate the uncertainty in the process of drop landing. However, to quantify the range effectively, multiple measurements are carried out and the value of the standard deviation that will be presented in the work combines the uncertainty due to drop landing effects, local surface changes and goniometer measurement uncertainty (Type A + Type B).

Capillary wicking was also estimated in the present work to characterize the hydrophilic samples after gamma irradiation. Capillary wicking was measured using high-speed imaging of the volume of water absorbed by the surface which equals the decrease in volume in a capillary tube. The method of capillary wicking measurement is described by Ahn et al.[48] A pendant drop is created at the end of a capillary tube and the surface to be tested is translated upward to touch the drop.

The volume absorbed per unit time is taken as the characteristic of capillary wicking in the present case. The experimental uncertainty in the measurement of the wicking velocity is estimated as 0.1 mm^3/s. The measurement uncertainty is calculated as explained in Rahman et al.[49]

Surface Morphology and Chemistry

In order to measure the surface morphology and pore structure, a Zeiss Merlin Scanning electron microscope was used. The microscopic image of the surface was further processed to study the pore size and structure. A high-resolution electron detector was used with a voltage of 15kV to obtain images. Energy dispersive spectroscopy (EDS) and X-ray photoelectron spectroscopy (XPS, Physical Electronics Versaprobe II) survey scans were used to obtain the elemental composition of the tested samples. The composition of the sample used in the present work as measured with EDS were Zircaloy (1.32Sn-0.21Fe-0.11Cr-0.13O-BalZr.), 316-Stainless steel (0.016C,16.58Cr,2.01Mo,10.14Ni,0.067N,1.7Mn,0.48Si,0.12Cu, Bal Fe) and 110 Copper (0.09 O, Bal Cu).

Electrochemical potential measurement was also carried out to analyze changes in the oxide layer chemistry upon irradiation. Samples were inserted in an electrochemical solution comprising of 0.1M H2SO4 as electrolyte and a standard calomel electrode (SCE) as a reference electrode. The electrochemical potential was observed with reference to the SCE and later converted with a reference to the standard hydrogen electrode (SHE).

Quenching studies

The details of the quenching experiment are described in some of the previous works.[28, 77, 97] The tested samples are cylindrical rodlets which are heated in a radiant furnace powered by a

DC supply. The samples are quenched by dropping the sample from the furnace into the quenching pool of liquid water maintained at a constant temperature by means of a pneumatic pressure supply. The centerline temperature of the rodlet is recorded online using a thermocouple connected to a data acquisition system.

Results and Discussion

Effect of Irradiation on the Contact Angle

Surfaces were exposed to two different cumulative doses (Test I and Test II) in the gamma cells at SNL and MIT. Surfaces were placed in aluminum trays and covered with UHV foil to prevent the collection of dust or gross contaminants inside the gamma cells. This would isolate changes due to the electrochemical potential that would happen due to the exchange of ions when the sample surface contacts the metallic surface of the gamma cell. It should be noted that the surfaces were removed from the gamma cell once the contact angle measurement was carried out. Hence, numerous samples for each test (6 samples in this case) were initially loaded and one sample was taken out for each exposure length during the total exposure time to carry out the contact angle measurement. This was done to minimize the impact of surface residue that could remain on the surface after exposure to the contact angle fluids. Fig. 2 shows the changes in contact angle for the four different fluids tested. It can be seen that for all fluids, the contact angle decreased with exposure. It should be recalled that the possible mechanism for decreased CA in with gamma exposure that were discussed earlier were photon-induced anodic reaction between water molecules[75] or local oxidation [77] occurring as a result of surface exposure to ionizing

radiation.

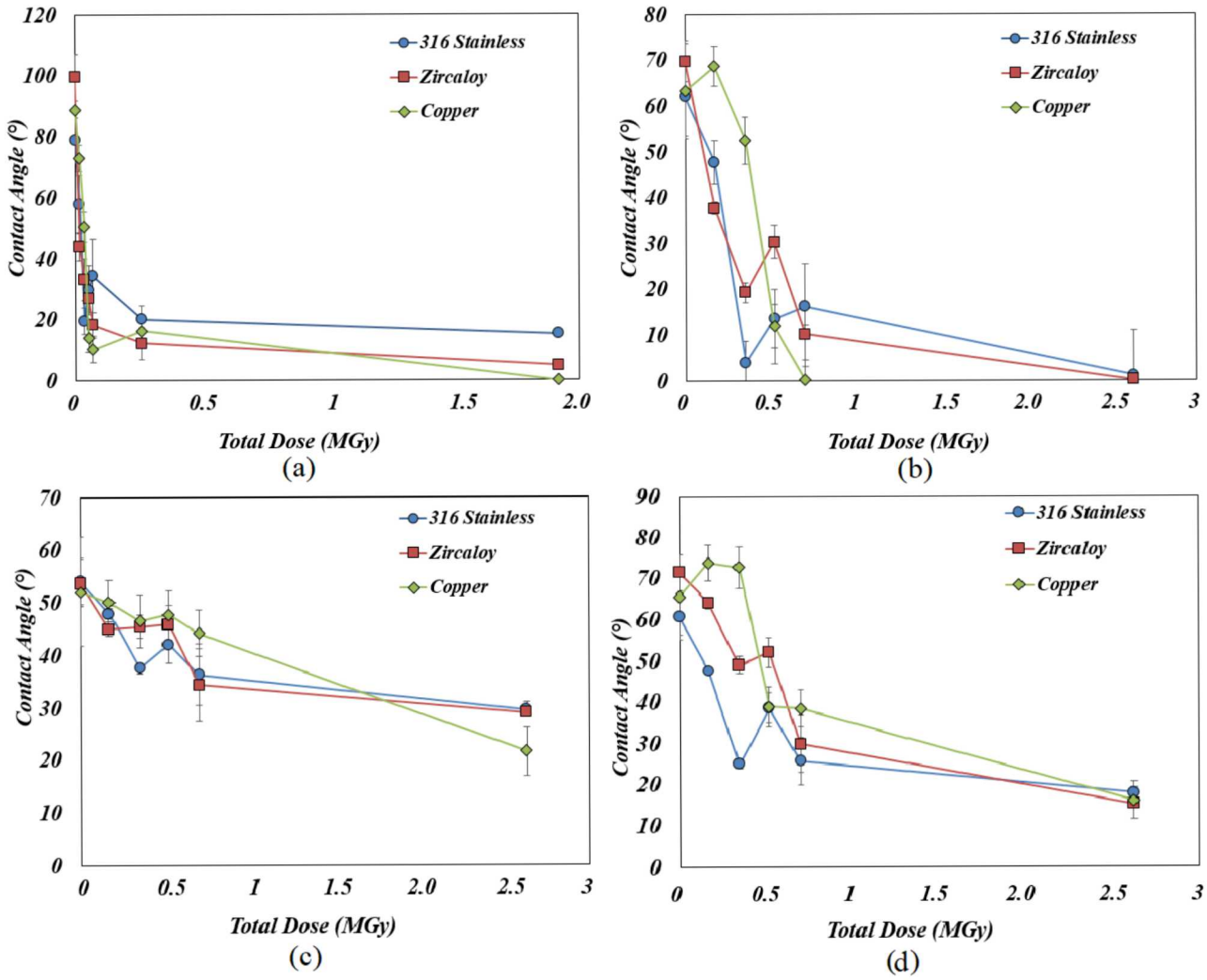

Figure 2. (a) deionized water (b) ethylene glycol (c) diiodomethane (d) glycerol

It can also be seen from Fig. 3 that the contact angle measurements carried out after exposing the samples at two different dose rates are in good agreement. This is a clear indication that the increased wettability depends on the cumulative dose and not on the dose rate. The important conclusion from the work is similar to the observation on non-ionizing laser irradiation. Gregorčič,

et al. [98] demonstrated that total absorbed energy by the laser irradiation impacts the wettability and not the pattern or rate of exposure It is also seen from Fig. 3 that the wettability change for water saturates around 10-20° depending on the sample. However, when exposed to very high dose of 19.2 MGy, copper exhibited superhydrophillicity (CA < ~5° , not saturated Wenzel regime). Considerable damage to the copper surface was observed at high cumulative dose both in the visual examination and microscopic measurements (as discussed later). This surface damage in copper was also observed in the low dose rate experiments carried out at MIT and needs further electrochemical assessment to analyze the cause of surface damage.

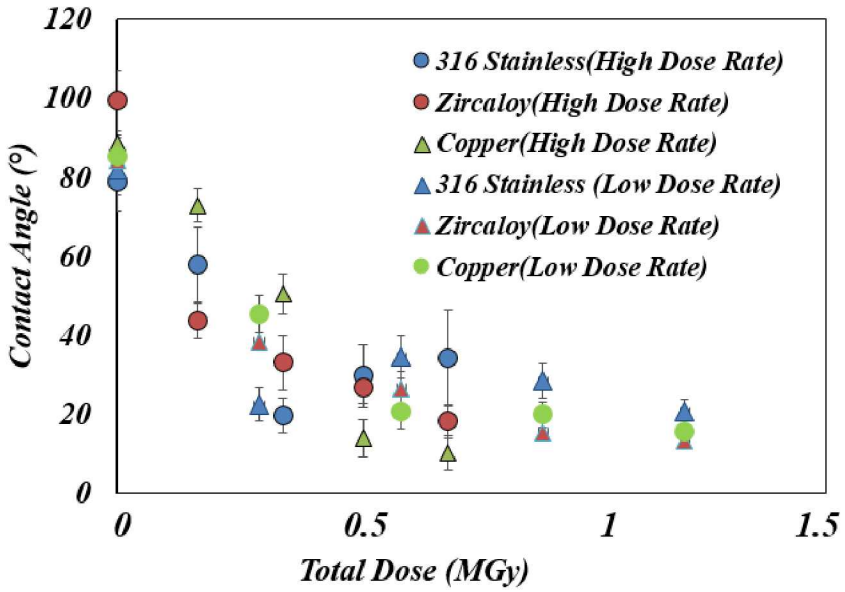

Figure 3. Wettability enhancement observed (a) for two different dose rates and for different fluids

Following exposure, the sample remained within the UHV foil wrap and were kept in a laboratory environment. It was seen that the samples retained the increased hydrophilic state even after 7 days, with contact angles in the same range as values when tested immediately after gamma

exposure. However, when samples were unwrapped and kept in the open atmosphere, there was an increase in the contact angle. This phenomenon, called hydrophobic recovery [99, 100], was described by the authors earlier [77] as well as by Takamasa, et al. [75] However, from the present study, it is concluded that this hydrophobic recovery happens only when the surface is exposed to gross contaminants and organics in the open environment and not after discontinuation of gamma irradiation. It is likely that the surface-activated UHV aluminum foil packaging served as a getter and reduced the contamination of sample surfaces when packaged. Similar recovery behavior was observed earlier in several works when laser textured surfaces were exposed to the ambient environment[58, 101, 102]. Transition to superhydrophobicity was observed in these works when the samples were exposed to the ambient environment for a prolonged period of time demonstrating a clear transition from Wenzel to Cassie-Baxter state. However, in the present work authors do not observe the transition to a superhydrophobic state (as observed in [103]) even after prolonged exposure to ambient air for 4 weeks. The recovered CA values were closer to the original CA values of the samples before irradiation. Table 2 summarizes the contact angle of the tested surfaces under various conditions during and after the exposure. The present observation on hydrophobic recovery also stresses the fact which was discussed by the authors previously [77], that the gamma-induced hydrophilicity is a permanent effect (unless counteracted by re-adsorption of atmospheric organic contaminants) and the increased hydrophilicity in the sample is sustained even after the discontinuation of exposure to gamma irradiation. Though the actual mechanism behind the recovery is still debated [103-105], based on the XPS surveys of the irradiated materials (see Fig S.1, supplementary material) as well as earlier report by the authors [77], it is reasonable to conclude that the organic contaminants in the ambient environment are responsible for the hydrophobic recovery. This is in contrast to the existing hypothesis that postulates the temporary

nature of radiation-induced surface activation.[71] The role of contamination on wettability has already been addressed in detail by the author.[106]. The surface can also be contaminated from prolonged exposure to the boiling heat transfer environment. This type of contamination can also impact the hydrophobic recovery rate of the material surface [17, 107].

Table 2. Water Contact angle of tested samples at different conditions

Sample	**Sample Condition**	**Average Contact Angle (°) and standard deviation**
Zircaloy-4	As polished	99.4 (4.6)
	Irradiated (2.63 MGy)	12.2 (2.5)
	Wrapped in UHV foil (7 days after irradiation)	15.9 (3.3)
	Open Environment (48 hours)	76.6(4.4)
Copper	As polished	88.6(6.8)
	Irradiated (2.63 MGy)	16.2(1.7)
	Wrapped in UHV foil (7 days after irradiation)	20.4(2.4)
	Open Environment (48 hours)	84.6(1.7)
Stainless Steel	As polished	78.8(4.4)
	Irradiated (2.63 MGy)	20.1(1.4)
	Wrapped in UHV foil (7 days after irradiation)	19.8(2.8)
	Open Environment (48 hours)	79.4(7.2)

Surface Energy and Capillary Wicking Measurements

Surface energy measurements were carried out using the Owens-Wendt method only for the high dose rate experiments performed at SNL. Surface free energy on all the samples increased with cumulative dose as shown in Figure 4. The increase in surface energy with exposure was monotonic in most of the tests until a saturation effect was observed. There was a slight decrease in surface energy observed initially for copper. This was contrary to the trend observed in water contact angle measurement which had a monotonic decrease throughout the exposure length. Similarly, a non-monotonic change was observed at an intermediate dose for stainless steel which was also observed in the water contact angle measurement. The electrochemical potential analysis later in the paper provides an explanation behind such trends. The surface energy remained the same after the discontinuation of irradiation when the samples were covered with the UHV foil. As observed in the contact angle measurements, there was a dip in surface energy when the surface was brought in direct contact with the ambient environment. Considering the samples following irradiation were highly hydrophilic, a capillary wicking measurement was carried out. A recent analysis [28, 49] has provided evidentiary support on the impact of capillary wicking on CHF and two-phase heat transfer which motivated the authors to perform capillary wicking measurements on samples under different conditions. Table 2 summarizes the capillary wicking and surface energy values of different surface conditions. It can be seen that initially, non-wicking surfaces (unirradiated) become wicking surfaces upon exposure to gamma radiation and later revert to non-wicking surfaces due to hydrophobic recovery. However, the copper sample retains its wicking even after exposure to the environment due to more severe damage present on its surface relative to other samples. It can be seen from Table 2 and Table 3 that all three quantities (contact angle,

capillary wicking, and surface energy) showed similar trends and are in good agreement individually among all the samples.

Table 3. Surface energy and capillary wicking values for samples at different conditions

Sample	**Sample Condition**	**Surface Free Energy (mJ/m^2)**	**Capillary Wicking (mm^3/s)**
Zircaloy-4	As polished	34.26	0
	Irradiated (19.2 MGy)	66.33	6.54
	Wrapped in UHV foil	65.05	6.68
	Open Environment (36 hours)	41.16	0
Copper	As polished	35.27	0
	Irradiated (19.2 MGy)	67.52	12.24
	Wrapped in UHV foil	66.09	11.84
	Open Environment (36 hours)	46.17	10.28
Stainless Steel	As polished	35.36	0
	Irradiated (19.2 MGy)	63.68	4.82
	Wrapped in UHV foil	64.01	5.12
	Open Environment	36.41	0

	(36 hours)		
	Irradiated (19.2 MGy)	66.21	
	Wrapped in UHV foil	60.80	
	Open Environment (36 hours)	54.92	
	Open Environment (7 days)	34.61	

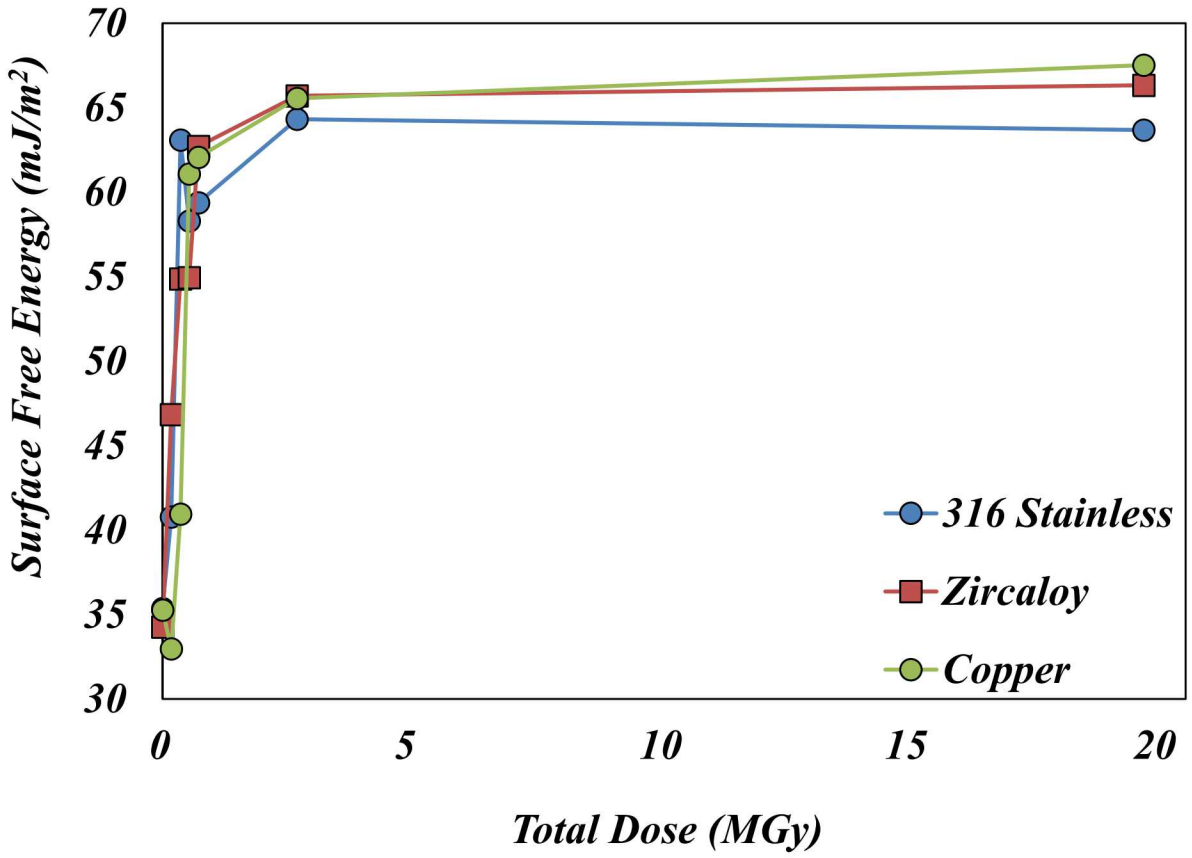

Figure 4. Surface energy measurement with gamma exposure

Surface Morphology and Electrochemical Studies

It is clear from the above analysis that the gamma irradiation induces a permanent change to the surfaces. In order to investigate this in detail, microscopic and electrochemical investigations were performed on the samples. Surfaces were observed before and after irradiation using scanning electron microscopy (SEM). Figure 5 shows the SEM images of the different surfaces before and after irradiation. It can be seen from the three figures that there were significant changes observed in the surface morphology upon irradiation. The SEM images of Zircaloy in Figure 5(a) shows that upon irradiation, localized pits/cracks form at different spatial locations. These pits had a high oxygen content when examined with EDS confirming that gamma irradiation resulted in localized oxidation. Such observations were reported earlier by several authors [108-113] in the presence of a corrosive liquid or environment. However, in the present work, this was observed even in the absence of a corrosive liquid. It is believed that the moisture in the ambient environment resulted in radiolysis and liberation of free oxygen ions leading to the accelerated localized corrosion. The observed local pits/cracks have a dimension of few microns initially and enlarge with an increase in dose rates as observed in the figures. These pits or cracks originated along the grain boundaries resulting from polishing. It has to be noted that no major change in the microstructure on any surface was observed when the surface was kept wrapped with aluminum foil after irradiation as one would expect and hence no SEM images are shown here. The pits were not observed in the SEM images after recovery. It is in agreement with the earlier elemental analysis of authors where organics were observed to cover the pits created during gamma irradiation [77].

The mechanism of corrosion as a result of gamma irradiation is observed to be intergranular in stainless steel as seen in Figure 5(b). Local oxidation starts at the grain boundaries and it

propagates with an increase in dose rates in stainless steel. At high dose rates, the intergranular corrosion propagates inside the grains. Similar pits and microcracks as Zircaloy also developed in copper upon irradiation as shown in Figure 5(c). These cracks also increase with radiation dose, however considerable damage to the surface appears upon irradiation as shown in the SEM images in Figure 5(c). Such damage was observed both in the high dose rate and low dose rate experiments. The reason for the extent of damage to the copper surface at very high dose rates is not known at this stage.

In all the three cases, both the EDS and XPS results show increased oxygen content with cumulative dose. The amount of oxygen as measured by EDS and XPS for different cumulative doses is plotted in Figure 6. There is a considerable difference in the values measured by EDS and XPS at different spatial locations arising from the spatial variation in oxidation. However, the magnitude and trends appear similar for both measurements confirming an increase in oxidation with cumulative dose.

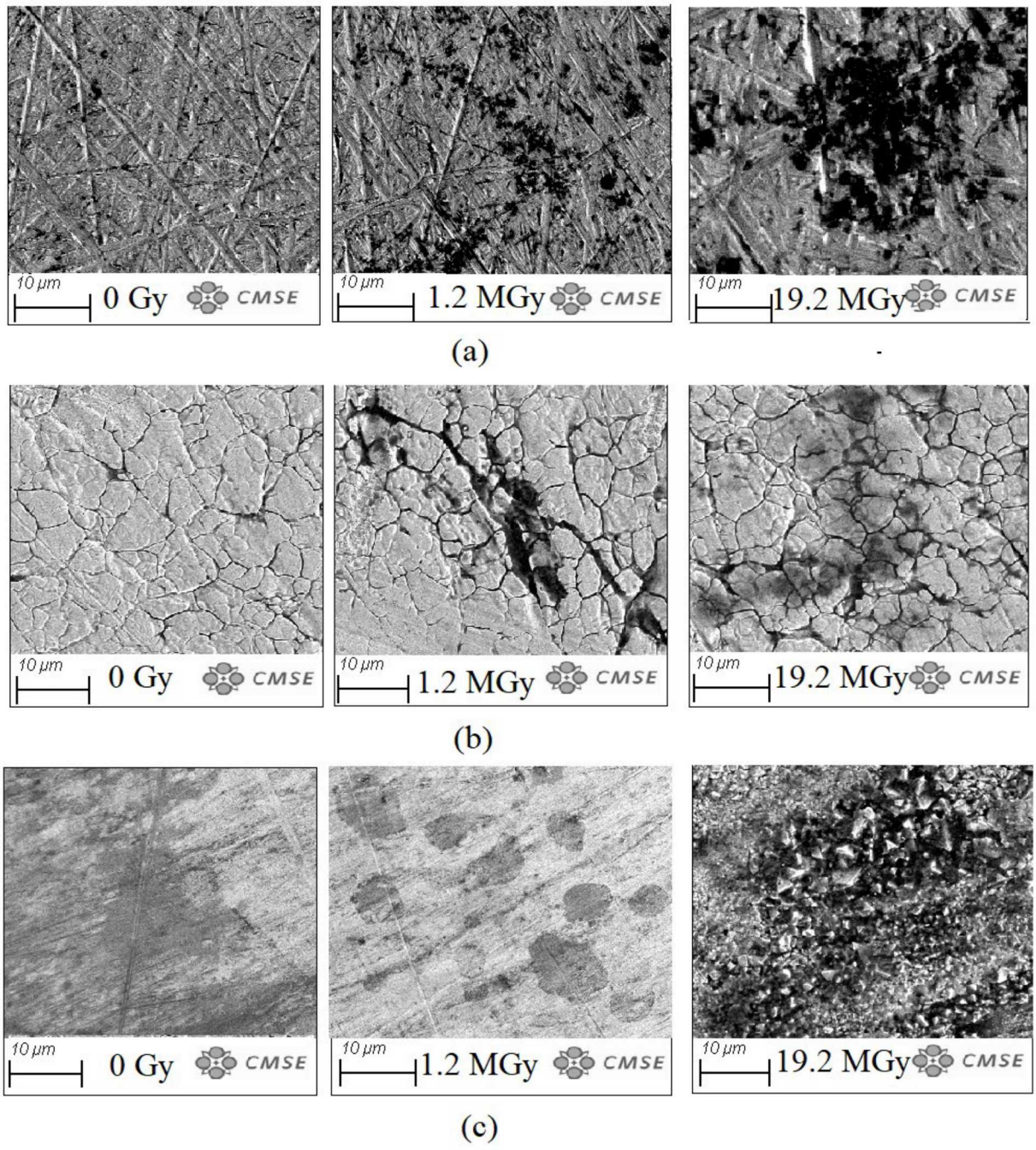

Figure 5. SEM observations at various stages in (a) Zircaloy-4 (b) stainless steel (c) copper

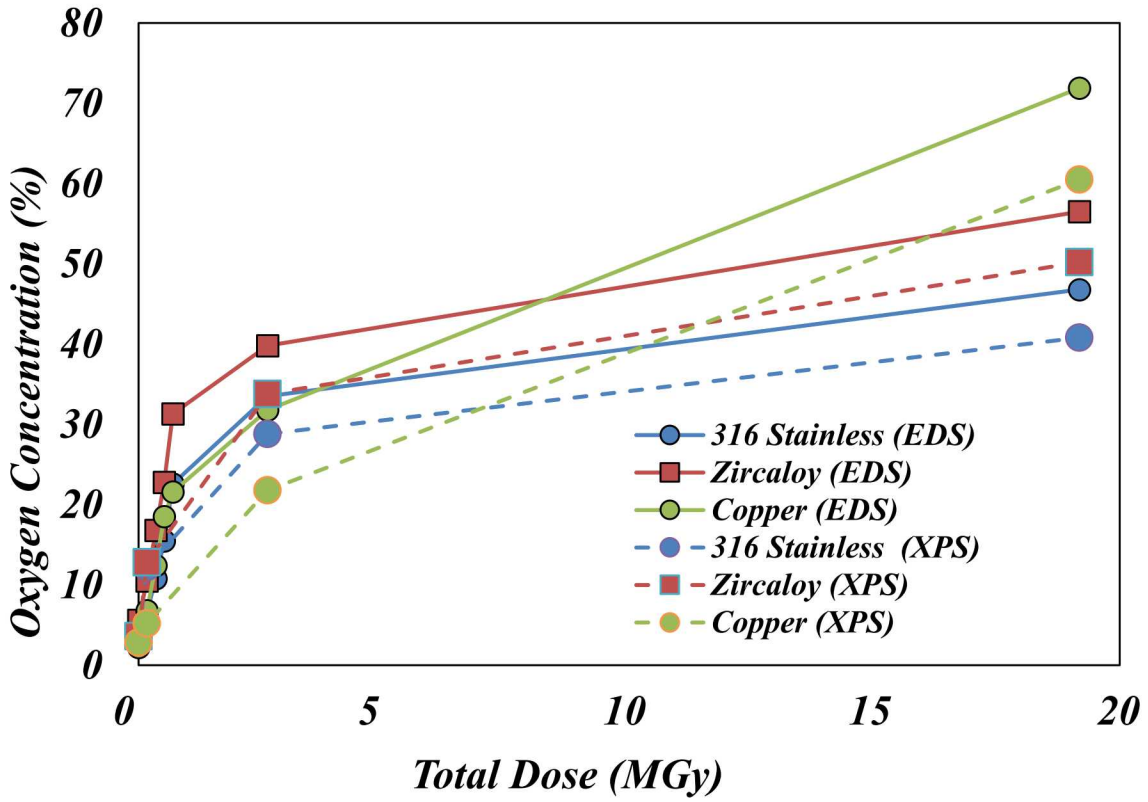

Figure 6. EDS and XPS measured oxygen concentration with cumulative dose

As mentioned earlier, the contact angle and surface energy change with increased exposure were monotonic in testing for all the samples except stainless steel and copper. At intermediate doses (0.5-0.7 MGy), stainless steel shows non-monotonic surface energy and contact angle variations. In order to investigate this further, the authors performed an open circuit electrochemical potential measurement on the samples at a different dose. This was done based on the understanding that at different stages of oxidation, the electrochemical potential of the substrate varies as a result of the nature of the oxide layer that forms. The electrochemical variation with cumulative dose is shown in Figure 7. It can be seen that there is a significant variation in the electrochemical potential (compared to SHE) for different gamma radiation exposures.

ECP measurements performed on Zircaloy showed a monotonic increase in ECP with dose before it saturates on the formation of zirconium oxide shown in Equation (6). This is in close agreement with the surface energy and wettability measurements on Zircaloy, which displayed a monotonic increase with the dose. However, the electrochemical reaction occurring due to the oxidation of stainless steel is quite complex with three major chemical reactions taking place as shown in Equation (7), (8), and (9). The corresponding electrochemical potential values are also shown beside the reactions and are taken from Haynes.[114] Comparing Figure 5(b) and equations (7), (8), and (9), it can be deduced that the non-monotonic change in surface energy or contact angle is a result of the change in the nature of the oxide that forms on the intergranular spaces in stainless steel. With an increase in cumulative dose, there is an increase in ECP values. This increase was much lower in the initial stage which corresponds to the formation of compounds containing iron (II) oxide. At a cumulative dose around 0.5-0.7 MGy, the ECP potential corresponds to that formation of oxyhydroxides. However, at high dose, the ECP potential increases still and saturates, with the corresponding ECP predicting the formation of Fe^{3+} ions. Hence, the contact angle which is strictly affected by the surface chemistry arising due to the local oxidation, likely assumes a non-monotonic trend due to the formation of oxyhydrides at the surface. Another possibility is the formation of a stable iron (II, III) oxide layer at the intermediate doses which cause a slight increase in contact angle. This non-monotonic effect will be studied further in the future through XRD and electrochemical impedance measurements.

Similarly, it can be seen from Figure 7(c) that the initial decrease in surface energy in copper is a result of positive electrochemical potential of copper that prevents rapid oxidation of surfaces. With increased dose, the electrochemical potential of copper decreases as result of the oxidation reaction shown in Equation (10), leading to an increase in wettability before it becomes a constant.

Equations:

$$Zr(s) \rightleftharpoons Zr^{2+} + 2e^{-} \quad (E^{corr} = -0.1 \text{ V SHE}) \tag{6}$$

$$Fe(s) \rightleftharpoons Fe^{2+} + 2e^{-} \quad (E^{corr} = -0.44 \text{ V SHE}) \tag{7}$$

$$Fe^{2+} + 2H_2O \rightleftharpoons FeOOH + 3H^{+} \quad (E^{corr} = -0.44 \text{ V SHE}) \tag{8}$$

$$3Fe^{2+} \rightleftharpoons 2Fe^{3+} + 3e^{-} \quad (E^{corr} = -0.44 \text{ V SHE}) \tag{9}$$

$$Cu \rightleftharpoons Cu^{2+} + 2e^{-} \quad (E^{corr} = -0.33 \text{ V SHE}) \tag{10}$$

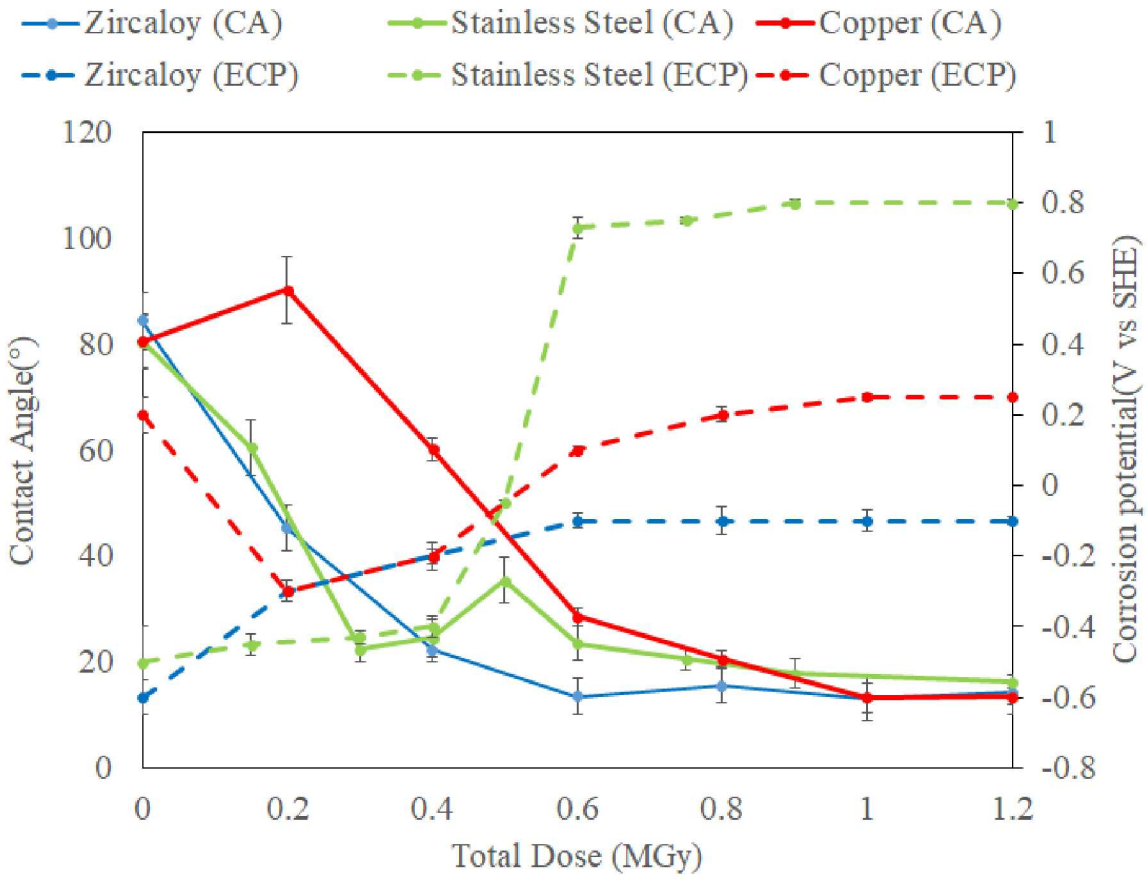

Figure 7. ECP measurements and water contact angle versus dose in the tested samples

Therefore, it is reasonable to conclude that local oxidation of different metals as a result of ionizing irradiation induced radiolysis is the mechanism responsible for the measured increase in surface energy. This mechanism is unique to the material and tested environment for ionizing irradiation. It is worth noting that several other authors have reported similar improved level of hydrophilicity due to texturing of materials with femtosecond and nanosecond non-ionizing Laser irradiations [58, 98, 115].

Quenching Experiments

A detailed study on the effect of gamma irradiation on quenching was already presented by the authors.[77] However, in order to understand the impact of cumulative dose on the quenching behavior, an uncoated Zircaloy sample and a Zircaloy sample coated with FeCrAl were investigated. The coating was applied on the substrate to understand the behavior of two samples without changing their thermal properties such as specific heat capacity. FeCrAl is chosen instead of stainless steel because of its higher potential as an accident tolerant fuel in LWR reactors [116, 117] A detailed report on the surface roughness, Leidenfrost temperature and quench front speed observed for the samples exposed to different cumulative doses is shown in Table 4. Leidenfrost temperature and quench front speed are two important parameters in two-phase heat transfer analysis as explained earlier.

It can be seen from Table 4 that with an increase in cumulative dose there is a slight increase in surface roughness and capillary wicking which lead to an increased Leidenfrost temperature and quench front speed. Thus, the increase in surface energy in the previous section does translate in an improved in two-phase heat transfer. Comparing the applied cumulative dose to the gamma flux in an LWR, it can be concluded that increasing cumulative dose will have a positive impact

on the two-phase heat transfer and should be considered in modeling and design of light water reactors to improve the thermal margin.

Table 4: Quench results for irradiated samples

Sample	Surface Roughness (µm)	Leidenfrost Temperature (°C)	Quench front speed	Pore structure (SEM)	Wicking (mm^3/s)
Zirc-4 (0.4 MGy)	0.35	315	10.6	Micropores/Nanopores	5.42
FeCrAl (0.4 MGy)	0.38	343	12.8	Micropores/ Nanopores	7.53
Zirc-4 (19.2 MGy)	0.42	324	13.2	Large patches	7.21
FeCrAl (19.2 MGy)	0.48	352	14.4	Numerous nanopores Some patches	9.53

Conclusion

A comprehensive study on the effect of gamma irradiation on surface wettability and morphology change was carried out at gamma irradiation facilities with different dose rates. It was seen from the analysis that the cumulative dose had a significant impact in the wettability and the effect of dose rate can be neglected. The contact angle measurement after recovery and comprehensive microscopic examination of surfaces overruled the existing hypothesis that the hydrophilic effect of gamma irradiation is temporary. As an ionizing radiation, Gamma rays induce radiolysis of water molecules in ambient air and are observed to cause local oxidation, pitting, and corrosion even in the absence of corrosive reagents or high temperature environments, depending on the material substrate. The local oxidation appears to increase with an increase in the cumulative dose, thereby increasing the surface energy and wettability of the surfaces. At high cumulative dose, there was a significant increase in the surface roughness and pore formation resulting from the irradiation, leading to improved capillary wicking. This increase in capillary wicking is observed to play a vital role in the improvement in quenching. The contact angle or surface energy is also impacted by the nature of oxide film as was observed from the electrochemical potential measurements carried out on various substrates which indicates a clear relation between the oxidation kinetics and contact angle variation. The impact of localized corrosion on the oxidation rate and two-phase flow dynamics for different applications should be studied in the future with associated electrochemical potential and XRD studies.

Acknowledgments

Maryla Wasiolek and Don Hanson (Sandia) are gratefully acknowledged for supporting the irradiation campaigns at the GIF.

This work was supported by the U.S. Department of Energy, Office of Nuclear Energy under DOE Idaho Operations Office Contract DE-AC07- 051D14517 as part of a Nuclear Science User Facilities experiment.

Sandia National Laboratories is a multimission laboratory managed and operated by National Technology & Engineering Solutions of Sandia, LLC, a wholly owned subsidiary of Honeywell International Inc., for the U.S. Department of Energy's National Nuclear Security Administration under contract DE-NA0003525.

This paper describes objective technical results and analysis. Any subjective views or opinions that might be expressed in the paper do not necessarily represent the views of the U.S. Department of Energy or the United States Government. Unclassified, unlimited release, SAND2019-XXXX.

References

[1] H. Hu, C. Xu, Y. Zhao, K.J. Ziegler, J.N. Chung, Boiling and quenching heat transfer advancement by nanoscale surface modification, Scientific Reports, 7 (2017).
[2] S.M. Ghiaasiaan, Two-phase flow, boiling, and condensation: in conventional and miniature systems, Cambridge University Press2007.
[3] J.G. Collier, J.R. Thome, Convective boiling and condensation, Clarendon Press1994.
[4] S.G. Kandlikar, Handbook of phase change: boiling and condensation, Routledge2018.
[5] W. Jiang, C. Yang, Y. Zhu, Y. Liu, H. Lu, B. Liang, Separation application of superhydrophobic Cu gauze to a non-aqueous system: Biodiesel collection from glycerol/FAME two-phase mixture, Applied Surface Science, 457 (2018) 456-467.
[6] J.R. Lamarsh, A.J. Baratta, Introduction to nuclear engineering, Prentice hall Upper Saddle River, NJ2001.
[7] J.A. Boure, A.E. Bergles, L.S. Tong, Review of two-phase flow instability, Nuclear Engineering and Design, 25 (1973) 165-192.
[8] M. Andreani, G. Yadigaroglu, Prediction methods for dispersed flow film boiling, International journal of multiphase flow, 20 (1994) 1-51.
[9] H. Kim, G. DeWitt, T. McKrell, J. Buongiorno, L.-w. Hu, On the quenching of steel and zircaloy spheres in water-based nanofluids with alumina, silica and diamond nanoparticles, International Journal of Multiphase Flow, 35 (2009) 427-438.
[10] L. Tong, BOILING CRISIS AND CRITICAL HEAT FLUX, Westinghouse Electric Corp., Pittsburgh, Pa., 1972.
[11] K.H. Chu, R. Enright, E.N. Wang, Structured surfaces for enhanced pool boiling heat transfer, Applied Physics Letters, 100 (2012).

[12] S.G. Kandlikar, A theoretical model to predict pool boiling CHF incorporating effects of contact angle and orientation, Journal of Heat Transfer, 123 (2001) 1071-1079.
[13] D. Groeneveld, The minimum film boiling temperature for water during film boiling collaps, Proc. 7th Int. Heat Tranfer Conf., 1982.
[14] H. Kim, J. Buongiorno, Detection of liquid–vapor–solid triple contact line in two-phase heat transfer phenomena using high-speed infrared thermometry, International Journal of Multiphase Flow, 37 (2011) 166-172.
[15] K. Baumeister, F. Simon, Leidenfrost temperature—its correlation for liquid metals, cryogens, hydrocarbons, and water, Journal of Heat Transfer, 95 (1973) 166-173.
[16] D.D. Hall, I. Mudawar, Critical heat flux (CHF) for water flow in tubes—I. Compilation and assessment of world CHF data, Int. J. Heat Mass Transf., 43 (2000) 2573-2604.
[17] M. Može, M. Zupančič, M. Hočevar, I. Golobič, P. Gregorčič, Surface chemistry and morphology transition induced by critical heat flux incipience on laser-textured copper surfaces, Applied Surface Science, 490 (2019) 220-230.
[18] C. Unal, R. Nelson, A PHENOMENOLOGICAL MODEL OF THE THERMAL-HYDRAULICS OF CONVECTIVE BOILING DURING THE QUENCHING OF HOT ROD BUNDLES .2. ASSESSMENT OF THE MODEL WITH STEADY-STATE AND TRANSIENT POST-CHF DATA, Nuclear Engineering and Design, 136 (1992) 299-318.
[19] A. Grounds, R. Still, K. Takashina, Enhanced droplet control by transition boiling, Scientific reports, 2 (2012) 720.
[20] C. Lee, H. Kim, H.S. Ahn, M.H. Kim, J. Kim, Micro/nanostructure evolution of zircaloy surface using anodization technique: Application to nuclear fuel cladding modification, Applied Surface Science, 258 (2012) 8724-8731.
[21] Y. Tang, B. Tang, J. Qing, Q. Li, L. Lu, Nanoporous metallic surface: Facile fabrication and enhancement of boiling heat transfer, Applied Surface Science, 258 (2012) 8747-8751.
[22] Y.-Q. Wang, S.-S. Lyu, J.-L. Luo, Z.-Y. Luo, Y.-X. Fu, Y. Heng, J.-H. Zhang, D.-C. Mo, Copper vertical micro dendrite fin arrays and their superior boiling heat transfer capability, Applied Surface Science, 422 (2017) 388-393.
[23] M. Zupančič, M. Može, P. Gregorčič, I. Golobič, Nanosecond laser texturing of uniformly and non-uniformly wettable micro structured metal surfaces for enhanced boiling heat transfer, Applied Surface Science, 399 (2017) 480-490.
[24] K. Sefiane, D. Benielli, A. Steinchen, A new mechanism for pool boiling crisis, recoil instability and contact angle influence, Colloids and Surfaces A: Physicochemical and Engineering Aspects, 142 (1998) 361-373.
[25] F. Zhang, A.M. Jacobi, Aluminum surface wettability changes by pool boiling of nanofluids, Colloids and Surfaces A: Physicochemical and Engineering Aspects, 506 (2016) 438-444.
[26] S.R. Chowdhury, R. Winterton, Surface effects in pool boiling, Int. J. Heat Mass Transf., 28 (1985) 1881-1889.
[27] H. Kim, B. Truong, J. Buongiorno, L.-W. Hu, On the effect of surface roughness height, wettability, and nanoporosity on Leidenfrost phenomena, Applied Physics Letters, 98 (2011) 083121.
[28] A. Seshadri, K. Shirvan, Quenching heat transfer analysis of accident tolerant coated fuel cladding, Nuclear Engineering and Design, 338 (2018) 5-15.

[29] E. Forrest, E. Williamson, J. Buongiorno, L.W. Hu, M. Rubner, R. Cohen, Augmentation of nucleate boiling heat transfer and critical heat flux using nanoparticle thin-film coatings, Int. J. Heat Mass Transf., 53 (2010) 58-67.
[30] J.S. Coursey, J. Kim, Nanofluid boiling: The effect of surface wettability, International Journal of Heat and Fluid Flow, 29 (2008) 1577-1585.
[31] S.J. Kim, I.C. Bang, J. Buongiorno, L.W. Hu, Effects of nanoparticle deposition on surface wettability influencing boiling heat transfer in nanofluids, Applied Physics Letters, 89 (2006).
[32] S.J. Kim, I.C. Bang, J. Buongiorno, L.W. Hu, Surface wettability change during pool boiling of nanofluids and its effect on critical heat flux, Int. J. Heat Mass Transf., 50 (2007) 4105-4116.
[33] S.G. Liter, M. Kaviany, Pool-boiling CHF enhancement by modulated porous-layer coating: Theory and experiment, Int. J. Heat Mass Transf., 44 (2001) 4287-4311.
[34] Z.h. Liu, J.g. Xiong, R. Bao, Boiling heat transfer characteristics of nanofluids in a flat heat pipe evaporator with micro-grooved heating surface, International Journal of Multiphase Flow, 33 (2007) 1284-1295.
[35] S.M. You, J.H. Kim, K.H. Kim, Effect of nanoparticles on critical heat flux of water in pool boiling heat transfer, Applied Physics Letters, 83 (2003) 3374-3376.
[36] P. Gregorčič, M. Zupančič, I. Golobič, Scalable surface microstructuring by a fiber laser for controlled nucleate boiling performance of high-and low-surface-tension fluids, Scientific reports, 8 (2018) 1-8.
[37] P. Zakšek, M. Zupančič, P. Gregorčič, I. Golobič, Investigation of Nucleate Pool Boiling of Saturated Pure Liquids and Ethanol-Water Mixtures on Smooth and Laser-Textured Surfaces, Nanoscale and Microscale Thermophysical Engineering, (2019) 1-14.
[38] M. Zupančič, M. Steinbücher, P. Gregorčič, I. Golobič, Enhanced pool-boiling heat transfer on laser-made hydrophobic/superhydrophilic polydimethylsiloxane-silica patterned surfaces, Applied Thermal Engineering, 91 (2015) 288-297.
[39] H.S. Ahn, H.J. Jo, S.H. Kang, M.H. Kim, Effect of liquid spreading due to nano/microstructures on the critical heat flux during pool boiling, Applied Physics Letters, 98 (2011).
[40] K.N. Rainey, S.M. You, Pool boiling heat transfer from plain and microporous, square pin-finned surfaces in saturated FC-72, Journal of Heat Transfer, 122 (2000) 509-516.
[41] N.S. Dhillon, J. Buongiorno, K.K. Varanasi, Critical heat flux maxima during boiling crisis on textured surfaces, Nature communications, 6 (2015) 1-12.
[42] H. O'Hanley, C. Coyle, J. Buongiorno, T. McKrell, L.W. Hu, M. Rubner, R. Cohen, Separate effects of surface roughness, wettability, and porosity on the boiling critical heat flux, Applied Physics Letters, 103 (2013).
[43] J.M. Kim, J.H. Kim, S.C. Park, M.H. Kim, H.S. Ahn, Nucleate boiling in graphene oxide colloids: Morphological change and critical heat flux enhancement, International Journal of Multiphase Flow, 85 (2016) 209-222.
[44] S. Mori, K. Okuyama, Enhancement of the critical heat flux in saturated pool boiling using honeycomb porous media, International Journal of Multiphase Flow, 35 (2009) 946-951.
[45] W. Zhang, Y. Chai, J. Xu, G. Liu, Y. Sun, 3D heterogeneous wetting microchannel surfaces for boiling heat transfer enhancement, Applied Surface Science, 457 (2018) 891-901.
[46] H. Fujimoto, Y. Oku, T. Ogihara, H. Takuda, Hydrodynamics and boiling phenomena of water droplets impinging on hot solid, International Journal of Multiphase Flow, 36 (2010) 620-642.

[47] K. Jun-young, L. Gi Cheol, M. Kaviany, P. Hyun Sun, K. Moriyama, K. Moo Hwan, Control of minimum film-boiling quench temperature of small spheres with micro-structured surface, International Journal of Multiphase Flow, 103 (2018) 30-42.
[48] H.S. Ahn, G. Park, J.M. Kim, J. Kim, M.H. Kim, The effect of water absorption on critical heat flux enhancement during pool boiling, Experimental Thermal and Fluid Science, 42 (2012) 187-195.
[49] M.M. Rahman, E. Olceroglu, M. McCarthy, Role of wickability on the critical heat flux of structured superhydrophilic surfaces, Langmuir, 30 (2014) 11225-11234.
[50] R.S. Hale, R.T. Bonnecaze, C.H. Hidrovo, Optimization of capillary flow through square micropillar arrays, International Journal of Multiphase Flow, 58 (2014) 39-51.
[51] M. Moeini Sedeh, J.M. Khodadadi, Interface behavior and void formation during infiltration of liquids into porous structures, International Journal of Multiphase Flow, 57 (2013) 49-65.
[52] N.K. Palakurthi, S. Konangi, U. Ghia, K. Comer, Micro-scale simulation of unidirectional capillary transport of wetting liquid through 3D fibrous porous media: Estimation of effective pore radii, International Journal of Multiphase Flow, 77 (2015) 48-57.
[53] M.F. Pucci, P.-J. Liotier, S. Drapier, Capillary wicking in flax fabrics – Effects of swelling in water, Colloids and Surfaces A: Physicochemical and Engineering Aspects, 498 (2016) 176-184.
[54] T.L. Staples, D.G. Shaffer, Wicking flow in irregular capillaries, Colloids and Surfaces A: Physicochemical and Engineering Aspects, 204 (2002) 239-250.
[55] A. Zou, D.P. Singh, S.C. Maroo, Early Evaporation of Microlayer for Boiling Heat Transfer Enhancement, Langmuir, 32 (2016) 10808-10814.
[56] A. Seshadri, K. Shirvan, Accelerating Introduction of Innovative Claddings Through Microscale Phenomenological Understanding of Thermal Hydraulics, ANS Winter Meeting 2019, American Nuclear Societty, Hilton Orlando, 2019.
[57] A.B.D. Cassie, S. Baxter, Wettability of porous surfaces, Transactions of the Faraday Society, 40 (1944) 546-551.
[58] P. Gregorčič, B. Šetina-Batič, M. Hočevar, Controlling the stainless steel surface wettability by nanosecond direct laser texturing at high fluences, Applied Physics A, 123 (2017) 766.
[59] A. Marmur, C. Della Volpe, S. Siboni, A. Amirfazli, J.W. Drelich, Contact angles and wettability: towards common and accurate terminology, Surface Innovations, 5 (2017) 3-8.
[60] G. McHale, N. Shirtcliffe, M. Newton, Super-hydrophobic and super-wetting surfaces: analytical potential?, Analyst, 129 (2004) 284-287.
[61] R.N. Wenzel, Resistance of solid surfaces to wetting by water, Industrial & Engineering Chemistry, 28 (1936) 988-994.
[62] B.J. Zhang, R. Ganguly, K.J. Kim, C.Y. Lee, Control of pool boiling heat transfer through photo-induced wettability change of titania nanotube arrayed surface, International Communications in Heat and Mass Transfer, 81 (2017) 124-130.
[63] W. Wang, D. Li, M. Tian, Y.-C. Lee, R. Yang, Wafer-scale fabrication of silicon nanowire arrays with controllable dimensions, Applied Surface Science, 258 (2012) 8649-8655.
[64] X. Chen, L. Song, X. Jiang, X. Zhang, Bioinspired superhydrophobic–superhydrophilic convertible film based on anisotropic red blood cell-like particles with protuberances, Colloids and Surfaces A: Physicochemical and Engineering Aspects, 579 (2019) 123674.
[65] Y. Liu, W. Liu, G. Wang, J. Huo, H. Kong, W. Wang, D. Wang, Z. Song, A facile one-step approach to superhydrophilic silica film with hierarchical structure using fluoroalkylsilane, Colloids and Surfaces A: Physicochemical and Engineering Aspects, 539 (2018) 109-115.

[66] B. Jiang, Z. Chen, H. Dou, Y. Sun, H. Zhang, Z.Q. Gong, L. Zhang, Superhydrophilic and underwater superoleophobic Ti foam with fluorinated hierarchical flower-like TiO2 nanostructures for effective oil-in-water emulsion separation, Applied Surface Science, 456 (2018) 114-123.
[67] H. Qian, J. Yang, Y. Lou, O. ur Rahman, Z. Li, X. Ding, J. Gao, C. Du, D. Zhang, Mussel-inspired superhydrophilic surface with enhanced antimicrobial properties under immersed and atmospheric conditions, Applied Surface Science, 465 (2019) 267-278.
[68] M. Li, T. Deng, S. Liu, F. Zhang, G. Zhang, Superhydrophilic surface modification of fabric via coating with nano-TiO2 by UV and alkaline treatment, Applied Surface Science, 297 (2014) 147-152.
[69] R. Dong, X. Jiang, C. Hao, W. Xu, H. Li, Y. Chen, T. Xie, Wettability of quartz controlled by UV light irradiation using an azobenzene surfactant, Colloids and Surfaces A: Physicochemical and Engineering Aspects, 578 (2019) 123586.
[70] J. Voglar, P. Gregorčič, M. Zupančič, I. Golobič, Boiling performance on surfaces with capillary-length-spaced one-and two-dimensional laser-textured patterns, International Journal of Heat and Mass Transfer, 127 (2018) 1188-1196.
[71] T. Takamasa, T. Hazuku, K. Okamoto, K. Mishima, M. Furuya, Radiation method surface activation on Leidenfrost and quenching phenomena, Experimental Thermal and Fluid Science, 29 (2005) 267-274.
[72] C. O'Connell, R. Sherlock, M.D. Ball, B. Aszalós-Kiss, U. Prendergast, T.J. Glynn, Investigation of the hydrophobic recovery of various polymeric biomaterials after 172nm UV treatment using contact angle, surface free energy and XPS measurements, Applied Surface Science, 255 (2009) 4405-4413.
[73] E.A. Waddell, S. Shreeves, H. Carrell, C. Perry, B.A. Reid, J. McKee, Surface modification of Sylgard 184 polydimethylsiloxane by 254nm excimer radiation and characterization by contact angle goniometry, infrared spectroscopy, atomic force and scanning electron microscopy, Applied Surface Science, 254 (2008) 5314-5318.
[74] J.K. Shim, H.S. Na, Y.M. Lee, H. Huh, Y.C. Nho, Surface modification of polypropylene membranes by γ-ray induced graft copolymerization and their solute permeation characteristics, Journal of Membrane Science, 190 (2001) 215-226.
[75] T. Takamasa, T. Hazuku, K. Mishima, K. Okamoto, Y. Imai, Surface wettability caused by radiation induced surface activation, Thermal Science and Engineering, 12 (2004) 39-44.
[76] H.G. Gong, A.R. Khan, N. Erkan, L.S. Wang, K. Okamoto, Critical heat flux enhancement in downward-facing pool boiling with radiation induced surface activation effect, Int. J. Heat Mass Transf., 109 (2017) 93-102.
[77] A. Seshadri, B. Phillips, K. Shirvan, Towards understanding the effects of irradiation on quenching heat transfer, Int. J. Heat Mass Transf., 127 (2018) 1087-1095.
[78] M. Bonelli, A. Miotello, P. Mosaner, Morphological changes induced on aluminum surfaces by excimer laser irradiation, Applied Surface Science, 186 (2002) 211-215.
[79] H. Jiang, Z. Duan, X. Zhao, B. Zhang, P. Wang, Influence of ions irradiation on the microstructural evolution, mechanical and tribological properties of Zr-4 alloy, Applied Surface Science, (2019) 143821.
[80] D.-H. Kim, D.-H. Lee, Effect of irradiation on the surface morphology of nanostructured superhydrophobic surfaces fabricated by ion beam irradiation, Applied Surface Science, 477 (2019) 154-158.

[81] E. Rui, J. Yang, X. Li, C. Liu, Change of surface morphology and structure of multi-walled carbon nanotubes film caused by proton irradiation with 170keV, Applied Surface Science, 287 (2013) 172-177.
[82] S. Yang, Z. Guo, L. Zhao, L. Zhao, Q. Guan, Y. Liu, Surface microstructures and high-temperature high-pressure corrosion behavior of N18 zirconium alloy induced by high current pulsed electron beam irradiation, Applied Surface Science, 484 (2019) 453-460.
[83] M.R. Murty, T. Curcic, A. Judy, B. Cooper, A. Woll, J. Brock, S. Kycia, R. Headrick, X-ray scattering study of the surface morphology of Au (111) during Ar+ ion irradiation, Physical review letters, 80 (1998) 4713.
[84] M. Miyauchi, N. Kieda, S. Hishita, T. Mitsuhashi, A. Nakajima, T. Watanabe, K. Hashimoto, Reversible wettability control of TiO2 surface by light irradiation, Surface Science, 511 (2002) 401-407.
[85] A. Borowiec, H. Haugen, Subwavelength ripple formation on the surfaces of compound semiconductors irradiated with femtosecond laser pulses, Applied Physics Letters, 82 (2003) 4462-4464.
[86] X. Zhu, M. Lei, T. Ma, Surface morphology of titanium irradiated by high-intensity pulsed ion beam, Nuclear Instruments and Methods in Physics Research Section B: Beam Interactions with Materials and Atoms, 211 (2003) 69-79.
[87] Y. Rosenberg, A. Siegmann, M. Narkis, S. Shkolnik, The sol/gel contribution to the behavior of γ-irradiated poly (vinylidene fluoride), Journal of applied polymer science, 43 (1991) 535-541.
[88] E.O. Zayim, N.D. Baydogan, Irradiation effect in WO3 thin films, Solar energy materials and solar cells, 90 (2006) 402-413.
[89] T. Young, Phil. Trans. Roy. Soc, (1805).
[90] A. Dupré, P. Dupré, Théorie mécanique de la chaleur, Gauthier-Villars1869.
[91] G. Azimi, R. Dhiman, H.-M. Kwon, A.T. Paxson, K.K. Varanasi, Hydrophobicity of rare-earth oxide ceramics, Nature materials, 12 (2013) 315.
[92] M.-N. Bellon-Fontaine, N. Mozes, H. Van der Mei, J. Sjollema, O. Cerf, P. Rouxhet, H. Busscher, A comparison of thermodynamic approaches to predict the adhesion of dairy microorganisms to solid substrata, Cell Biophysics, 17 (1990) 93.
[93] C. Van Oss, L. Ju, M. Chaudhury, R. Good, Estimation of the polar parameters of the surface tension of liquids by contact angle measurements on gels, Journal of Colloid and Interface Science, 128 (1989) 313-319.
[94] D.K. Owens, R. Wendt, Estimation of the surface free energy of polymers, Journal of applied polymer science, 13 (1969) 1741-1747.
[95] L. Girifalco, R.J. Good, A theory for the estimation of surface and interfacial energies. I. Derivation and application to interfacial tension, The Journal of Physical Chemistry, 61 (1957) 904-909.
[96] C.J. Van Oss, M.K. Chaudhury, R.J. Good, Interfacial Lifshitz-van der Waals and polar interactions in macroscopic systems, Chemical Reviews, 88 (1988) 927-941.
[97] H. Kim, J. Buongiorno, L.W. Hu, T. McKrell, Nanoparticle deposition effects on the minimum heat flux point and quench front speed during quenching in water-based alumina nanofluids, Int. J. Heat Mass Transf., 53 (2010) 1542-1553.
[98] P. Gregorčič, M. Conradi, L. Hribar, M. Hočevar, Long-term influence of laser-processing parameters on (super) hydrophobicity development and stability of stainless-steel surfaces, Materials, 11 (2018) 2240.

[99] J. Kim, M.K. Chaudhury, M.J. Owen, Hydrophobic recovery of polydimethylsiloxane elastomer exposed to partial electrical discharge, Journal of Colloid and Interface Science, 226 (2000) 231-236.
[100] M. Morra, E. Occhiello, R. Marola, F. Garbassi, P. Humphrey, D. Johnson, On the aging of oxygen plasma-treated polydimethylsiloxane surfaces, Journal of Colloid and Interface Science, 137 (1990) 11-24.
[101] U. Trdan, M. Hočevar, P. Gregorčič, Transition from superhydrophilic to superhydrophobic state of laser textured stainless steel surface and its effect on corrosion resistance, Corrosion science, 123 (2017) 21-26.
[102] A.-M. Kietzig, S.G. Hatzikiriakos, P. Englezos, Patterned superhydrophobic metallic surfaces, Langmuir, 25 (2009) 4821-4827.
[103] D.V. Ta, A. Dunn, T.J. Wasley, R.W. Kay, J. Stringer, P.J. Smith, C. Connaughton, J.D. Shephard, Nanosecond laser textured superhydrophobic metallic surfaces and their chemical sensing applications, Applied Surface Science, 357 (2015) 248-254.
[104] J. Long, M. Zhong, P. Fan, D. Gong, H. Zhang, Wettability conversion of ultrafast laser structured copper surface, Journal of Laser Applications, 27 (2015) S29107.
[105] J. Long, M. Zhong, H. Zhang, P. Fan, Superhydrophilicity to superhydrophobicity transition of picosecond laser microstructured aluminum in ambient air, Journal of colloid and interface science, 441 (2015) 1-9.
[106] E. Forrest, R. Schulze, C. Liu, D. Dombrowski, Influence of surface contamination on the wettability of heat transfer surfaces, International Journal of Heat and Mass Transfer, 91 (2015) 311-317.
[107] H. Yan, M.R.B.A. Rashid, S.Y. Khew, F. Li, M. Hong, Wettability transition of laser textured brass surfaces inside different mediums, Applied Surface Science, 427 (2018) 369-375.
[108] M. Domae, H. Kawamura, D. Akutagawa, K. Hisamune, Y. Katsumura, Y. Muroya, Corrosion test of 304 stainless steel in hydrazine and methanol solutions at 320 °C under gamma-irradiation and gamma radiolysis of hydrazine and methanol, International Conference on Nuclear Engineering, Proceedings, ICONE, 2010, pp. 113-121.
[109] N. Fujita, C. Matsuura, K. Saigo, Irradiation-enhanced corrosion of carbon steel in high temperature water - In view of a cell formation induced by γ-rays, Radiation Physics and Chemistry, 58 (2000) 139-147.
[110] M. Haginuma, S. Ono, K. Takamori, K. Takeda, K. Tachibana, K. Ishigure, Effect of gamma-ray irradiation on corrosion and cobalt accumulation of type 304 stainless steel in high-temperature water in the presence of zinc ion, Nippon Genshiryoku Gakkaishi/Journal of the Atomic Energy Society of Japan, 40 (1998) 397-406.
[111] C. Kato, T. Sato, J. Nakano, F. Ueno, I. Yamagishi, M. Yamamoto, Localized corrosion behavior of stainless steel in the diluted artificial sea-water contacted with zeolite under gamma-ray irradiation, Transactions of the Atomic Energy Society of Japan, 14 (2015) 181-188.
[112] C. Liu, J. Wang, Z. Zhang, E.H. Han, W. Liu, D. Liang, Z. Yang, X. Cao, Effect of cumulative gamma irradiation on microstructure and corrosion behaviour of X65 low carbon steel, Journal of Materials Science and Technology, 34 (2018) 2131-2139.
[113] M. Tachibana, K. Ishida, Y. Wada, N. Ota, N. Shigenaka, Effects of gamma-ray irradiation on crevice corrosion repassivation potential of stainless steel in high temperature diluted simulated seawater†, Journal of Nuclear Science and Technology, 53 (2016) 981-991.
[114] W.M. Haynes, CRC handbook of chemistry and physics, CRC press2014.

[115] A.-M. Kietzig, M. Negar Mirvakili, S. Kamal, P. Englezos, S.G. Hatzikiriakos, Laser-patterned super-hydrophobic pure metallic substrates: Cassie to Wenzel wetting transitions, Journal of Adhesion Science and Technology, 25 (2011) 2789-2809.
[116] A. Seshadri, K. Shirvan, Wettability and Quench Characteristics of Zircaloy and FeCrAl Coating, Transactions of the American Nuclear Society, American Nuclear Society, 2017, pp. 1729-1731.
[117] M. Snead, L. Snead, K.A. Terrani, K.G. Field, A. Worrall, K.R. Robb, Y. Yamamoto, J. Powers, S. Dryepondt, B. Pint, Technology Implementation Plan ATF FeCrAl Cladding for LWR Application, ORNL/TM-2014-353, Oak Ridge National Laboratory (May 2014), (2014).